The final publication is available at

https://doi.org/10.1002/cctc.202001760

The limits of the confinement effect associated to cage topology on the control of the MTO selectivity

Pau Ferri, Chengeng Li, Cecilia Paris, Aida Rodríguez-Fernández, Manuel Moliner, Mercedes Boronat* and Avelino Corma*

P. Ferri, Dr. C. Li, Dr. C. Paris, A. Rodríguez-Fernández, Dr. M. Moliner, Dr. M. Boronat, Dr. A. Corma
Instituto de Tecnología Química, Universitat Politècnica de Valencia – Consejo Superior de Investigaciones Científicas (UPV-CSIC)
Av. Naranjos, s/n, 46022 Valencia (Spain)
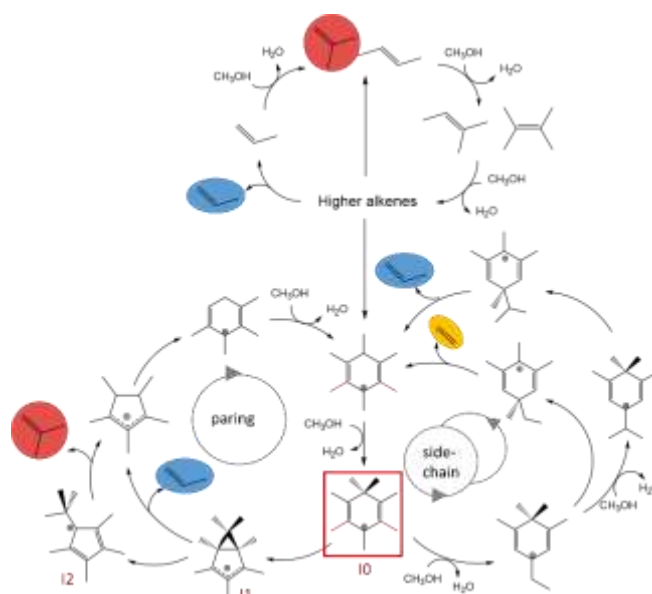E-mail: acorma@itq.upv.es, boronat@itq.upv.es

Supporting information for this article is given via a link at the end of the document

Abstract: The light olefin product distribution of the methanol-to-olefin (MTO) reaction catalyzed by acid zeolites and zeotypes depends on the nature of the entrapped hydrocarbon pool species that act as co-catalysts. The preferential stabilization by confinement effects of the cationic intermediates involved in the side-chain or paring pathways of the aromatics-based cycle of the MTO mechanism in small-pore cage-based zeolites is determined by the topology of the cavity, and can be quantitatively described through the $E_{int(7/5)}$ parameter obtained from DFT calculations. In this work we extend the study of the $E_{int(7/5)}$ parameter to a wide range of structures (ERI, LEV, AEI, CHA, DDR, AFX, RTH, ITE, SAV, UFI, RHO, KFI, and LTA) and discuss its applicability in small cages with steric constraints to host bulky intermediates, in zeolites with a tight fitting between the cavity and the hosted cations, and in large cages where confinement effects are lost in part and competitive processes occur.

Introduction

The methanol-to-olefins (MTO) reaction is a relevant process that produces short chain olefins such as ethene, propene and butene at industrial scale.[1-3] The commercial demand of these chemical products is nowadays fulfilled by steam cracking or fluidized catalytic cracking of higher hydrocarbons. The MTO reaction provides an alternative path for producing short chain olefins from sources such as coal, natural gas or biomass. In recent years, many MTO plants have emerged, being the coal-to-olefin plant built in China in 2010 the first one of its kind.[2]

The MTO reaction is catalyzed by acid zeolites (aluminosilicates) and SAPOs (silicoaluminophosphates) that can form, within their pores, organic molecules that act as co-catalysts. The true catalytic system comprises both the inorganic framework containing the Brønsted acid sites and the confined organic species, either alkenes or aromatics, that form the so-called "hydrocarbon pool" and produce light olefins by successive methylation and cracking steps.[4-7] The topology of the microporous structure determines the nature of the hydrocarbon pool species and, indirectly, the selectivity of the reaction.[4-17]

According to the widely accepted dual-cycle mechanism (Scheme 1), H-ZSM-5 favors the formation of propene and higher alkenes by methylation and cracking of alkenes in the 10-ring channels of the bidirectional system, while ethene production requires the participation, as hydrocarbon pool species, of aromatic alkylbenzenes allocated at the wider channels intersections.[5-7]

Scheme 1. Dual-cycle hydrocarbon pool mechanism proposed for the MTO reaction.

Suppression of the aromatics-based cycle in H-ZSM-22 topology containing only unidirectional 10-ring channels leads to a much lower production of ethene, while similar amounts of propene and ethene are obtained in the larger and interconnected 12-ring channels of H-BEA zeolite,[18] evidencing the influence of pore architecture not only on the formation of deactivating polycyclic aromatic hydrocarbon pool species which modify the catalyst lifetime,[19,20] but also on the light olefin product distribution.

In zeolite structures composed by relatively large cavities interconnected through small-pore 8-ring windows, such as H-SSZ-13 and H-SAPO-34 with the CHA topology, the hydrocarbon pool consists predominantly of aromatic polymethylbenzenes trapped within the internal cages, although some contribution of the alkene-based cycle cannot be ruled out completely.[8,9, 21- 24]

In the aromatics-based catalytic cycle, the selectivity to ethene, propene and butene depends on the relative contribution of the two possible competitive pathways included in the mechanism: the side-chain and paring routes (Scheme 1). [5-7, 16, 17, 25-28] Both routes share the same initial intermediate, a gem-methylated polymethylbenzenium cation (I0 in Scheme 1). The side-chain pathway starts with exo-methylation of I0 forming an alkyl chain that, after some methyl-shift steps, is eliminated yielding preferentially ethene. The paring route involves an initial ring

contraction of I0 to form a bicycle-hexenyl cation (I1 in Scheme 1) that splits off propene and, in a two-step process through an I2 intermediate, can additionally yield iso-butene. The resulting cyclopentenyl cations undergo subsequent ring-expansion and methylation steps to recover the hydrocarbon pool species. The evolution of the I0 intermediate toward the side-chain or the paring routes depends on the degree of methylation of the aromatic methylbenzene ring, with the ring-contraction step being energetically accessible only for highly methylated benzenium cations.[16] In this sense, the influence of pore architecture on product distribution is linked to the ability of each cage topology to host methylbenzene intermediates with a higher or lower degree of methylation.

The relationship between the degree of methylation of the aromatic hydrocarbon pool and the selectivity to ethene and propene was established by kinetic and isotopic labelling studies,[29-31] and the influence of cavity topology on light olefin product distribution was also demonstrated experimentally.[8-17] A large number of small-pore cage-based zeolites and SAPOs were systematically tested as catalysts for the MTO reaction by Davis et al. to establish a relationship between the MTO product distribution and the cavity topology described by a new parameter, the cage-defining ring size.[13-14] Fourteen crystallographic zeolite structures with different compositions were classified into four categories according to the relative amount of ethene, propene and butene formed, with the structures containing smaller cavities such as LEV and ERI producing more ethene than propene, and with butene appearing as an important product only in structures containing very large cavities such as SAV, LTA or RHO. However, it was not possible to establish a quantitative linear correlation between product distribution and either the diameter of the largest possible included sphere (D) or the cage-defining ring size.

All these observations were recently rationalized by combining DFT calculations with catalyst synthesis, characterization and testing.[15-17] A theoretical study of the paring mechanism for penta- and hepta-methylbenzene intermediates in CHA, AEI, RTH and ITE catalyst models showed a preferential stabilization of the fully-methylated species in RTH and ITE cavities, which would result in a higher contribution of the paring route and therefore a larger production of propene, in agreement with the catalytic results. In addition, a new descriptor, the $E_{int(7/5)}$ parameter, was defined from the DFT interaction energy of each cation within the different zeolite cavities to quantitatively describe the ability of a particular cage topology to host the fully methylated intermediates involved in the paring route.[16] A linear relationship was indeed observed between the $C_3^=/C_2^=$ ratios measured for different zeolites and the $E_{int(7/5)}$ parameter corresponding to each catalyst structure, thus confirming that the confinement effect associated to cage topology is probably the factor governing the MTO product selectivity. More recently, this parameter has been successfully applied to explain the different light olefin product distribution obtained with isostructural H-SSZ-13 and H-SAPO-34 catalysts, both of them with the CHA structure.[17] The larger flexibility of the silicoaluminophosphate material, which is correctly captured by the $E_{int(7/5)}$ parameter, allows the expansion of the cages necessary to accommodate the fully methylated intermediates, leading to an increased production of propene as compared to H-SSZ-13.

In this work we extend the study of the theoretical $E_{int(7/5)}$ parameter to a wider range of structures and chemical compositions used as MTO catalysts, including the smallest ERI and LEV cages where steric constraints might be present as well as large cavities such as those of SAV, RHO or LTA structures where the confinement effect might be lost. The final goal is to determine the scope of confinement effects for this process, and set the limits of the $E_{int(7/5)}$ parameter as predictor of product distribution in the MTO reaction.

Results and Discussion

According to the mechanism described in Scheme 1, the evolution of the gem-methylated I0 intermediate depends on its degree of ring-methylation.[15-17] The paring route is only accessible for the fully-methylated hepta-methylbenzenium (7MB+) cation, while the less substituted penta-methylbenzenium cation (5MB+) will follow the side-chain pathway. The relative concentration of each of these two key intermediates in different zeolite structures can be estimated from the interaction energies between the carbocationic species and the catalyst framework, through the $E_{int(7/5)}$ parameter calculated as $E_{int(7/5)} = E_{int(7MB+)}/E_{int(5MB+)}$.

The interaction energies of 7MB+ and 5MB+ intermediates with pure silica and pure aluminophosphate (AlPO) models of ERI, LEV, AEI, CHA, DDR, AFX, RTH, ITE, SAV, UFI, RHO, KFI, and LTA zeolite structures were estimated from periodic DFT calculations (Figure S1 and Table S1 in the Supporting Information) and used to obtain the $E_{int(7/5)}$ parameters summarized in Table 1. For comparison purposes, the diameter of the largest sphere that can be included in each structure (D) according to the IZA database[32] and the cage defining ring size (CDR) according to Davis[14] are also included in Table 1. At first sight, the three parameters used to characterize the cage topology follow the same trend: the smallest spheres are included in the smallest cage-defining rings, for which the smallest $E_{int(7/5)}$ values are obtained. As the diameter of the largest sphere included increases, the cage-defining ring size and $E_{int(7/5)}$ parameter increase too, with the exception of the AEI structure with a very particular cavity shape (see Figure S1). A deeper inspection of the values in Table 1 and the plot in Figure 1a clearly indicate that this trend is only valid for cavities with diameter D ≤ 9Å, that is, for the zeolite structures from ERI to SAV. In this range of cage dimensions, the composition of the framework (silicate or aluminophosphate) also plays a role in the stabilization of the entrapped carbocations, with the calculated $E_{int(7/5)}$ parameter always being larger for the AlPO materials. This is due in part to the slightly larger volume cell of the AlPO materials as compared to the isostructural zeolites, but the most important factor is the increased flexibility of the aluminophosphate framework with respect to that of silicate, which allows a less energy demanding expansion of the cavity that facilitates the accommodation of the bulkier 7MB+.[17] This effect is more pronounced in the smaller cavities (ERI, LEV, CHA) and diminishes when the architecture of the silicate cage is adequate to host 7MB+ without requiring too much distortion, as in AEI, AFX or SAV with $E_{int(7/5)}$ parameters close to 1.

For the wider cavities, UFI, RHO, KFI and LTA, the sphere included can be as large as 11,1 Å diameter and the cage-defining ring oscillates between 10.4 and 11.4 Å. However, the $E_{int(7/5)}$ parameter does not further increase and takes values slightly larger than unity, between 1.01 and 1.04, similar to those obtained for RTH and ITE and without any clear influence of framework

composition (see Table 1). The reason is that $E_{int(7/5)}$ is not just a geometric parameter such as the sphere diameter D or the cage-defining ring size, but it is based on the relative stabilization of 7MB+ and 5MB+ cations by van der Waals interactions with the zeolite framework. Too small cages such as those of ERI and LEV cannot accommodate the bulky 7MB+, so that the interaction energies calculated for 5MB+ are clearly larger than for 7MB+ (see Table S1) and the $E_{int(7/5)}$ values are lower than 1. But in too large cavities part of the confinement effect is lost because not all the methyl groups of the cationic intermediates can establish good contacts with the framework oxygen atoms. The optimized structures depicted in Figure 2 clearly show that the 7MB+ and 5MB+ cations usually stay in the center of the cavity in the structures with smaller cages, but tend to move close to the zeolite walls when the cavity dimensions do not fit those of the entrapped organic species. Thus, while 7MB+ cation occupies the center of the UFI cage, which is able to host a sphere of 10.1 Å diameter, the less methylated 5MB+ is displaced to one side of the cavity in order to achieve the largest number of close contacts with the framework. This displacement aiming to maximize the interactions with the framework is also observed for both 5MB+ and 7MB+ in the zeolite structures containing the largest cavities, such as RHO, KFI and LTA. In this situation, the bulkier 7MB+ is not much better stabilized than the less methylated 5MB+ and the calculated $E_{int(7/5)}$ parameter is ~1 regardless the size of the cage.

distribution may have a limit, which is reached when the shape and dimensions of the cavity do not fit the hosted species.

Table 1. Structural and energetic parameters used to characterize the cavity topology of small-pore cage-based zeolites used in the MTO reaction.

IZA code	D[a] (Å)	CDR[b] (Å)	$E_{int(7/5)}$ SiO$_2$	$E_{int(7/5)}$ AlPO	$E_{int(I2/I1)}$ SiO$_2$	$E_{int(I2/I1)}$ AlPO
ERI	7.04	6.76	0.807	0.852	0.982	1.020
LEV	7.10	7.15	0.822	0.896	0.911	0.878
AEI	7.33	8.52	0.997	1.000	0.960	0.947
CHA	7.37	7.45	0.933	0.946	0.954	0.958
DDR	7.66	7.07	0.955	-- [c]	0.946	-- [c]
AFX	7.76	7.44	0.987	0.995	0.978	0.980
RTH	8.18	9.00	1.018	-- [c]	0.973	-- [c]
ITE	8.30	9.11	1.012	-- [c]	0.974	-- [c]
SAV	8.82	9.60	1.036	1.042	1.007	1.000
UFI	10.09	10.45	1.017	-- [c]	0.980	-- [c]
RHO	10.43	11.41	1.016	1.009	0.997	1.010
KFI	10.67	10.67	1.045	1.029	0.999	1.005
LTA	11.05	10.44	1.001	1.022	1.001	1.003

[a] IZA Database of Zeolite Structures. [b] Data from ref. [14]. [c] No CIF available.

Table 2. Product selectivity at the same methanol conversion level (X=95%) for the different small pore zeolites and zeotypes and catalyst lifetime. Reaction conditions: T=623 or 673 K, WHSV=0.8 h^{-1}, w_{cat}=50 mg.

Sample	Comp.	Life time (min) X_{95}	Selectivity (%wt) $C_2^=$	$C_3^=$	$C_4^=$	$C_3^=/C_2^=$	$(C_4^=+C_3^=)/C_2^=$	$C_4^=/C_3^=$
[a]LEV	zeo	118	45.7	25.8	9.5	0.56	0.77	0.37
CHA_1	zeo	260	45.1	37.0	12.4	0.82	1.10	0.34
CHA_2	zeo	1085	47.1	34.2	12.1	0.73	0.98	0.35
CHA_3	SAPO	447	33.6	45.9	13.7	1.40	1.77	0.30
AEI_1	zeo	267	20.9	44.4	19.6	2.12	3.06	0.44
AEI_2	zeo	480	22.6	47.9	22.0	2.20	3.09	0.46
AEI_3	SAPO	138	22.9	47.8	21.0	2.09	3.00	0.44
AEI_4	SAPO	246	22.8	48.4	18.7	2.12	2.94	0.39
RTH_1	zeo	270	14.7	45.1	24.7	3.07	5.17	0.55
ITE	zeo	217	13.7	42.6	28.2	3.11	4.75	0.66
[b]LEV	zeo	354	51.9	21.5	9.8	0.41	0.60	0.46
CHA_1	zeo	670	56.4	30.4	9.2	0.54	0.70	0.30
CHA_3	SAPO	298	37.9	41.8	13.4	1.10	1.46	0.32
AEI_1	zeo	446	33.6	44.5	14.2	1.32	1.75	0.32
AEI_4	SAPO	471	34.5	46.4	13.2	1.34	1.73	0.28
RTH_1	zeo	236	27.6	44.2	16.8	1.60	2.80	0.38
RTH_2	zeo	105	26.9	42.9	14.8	1.60	2.21	0.34
ITE	zeo	378	24.4	47.8	20.6	1.95	2.14	0.43
LTA	zeo	-- [c]	28.3	32.2	16.4	1.14	1.72	0.51

[a] 623 K. [b] 673 K. [c] Product selectivity at 75% methanol conversion
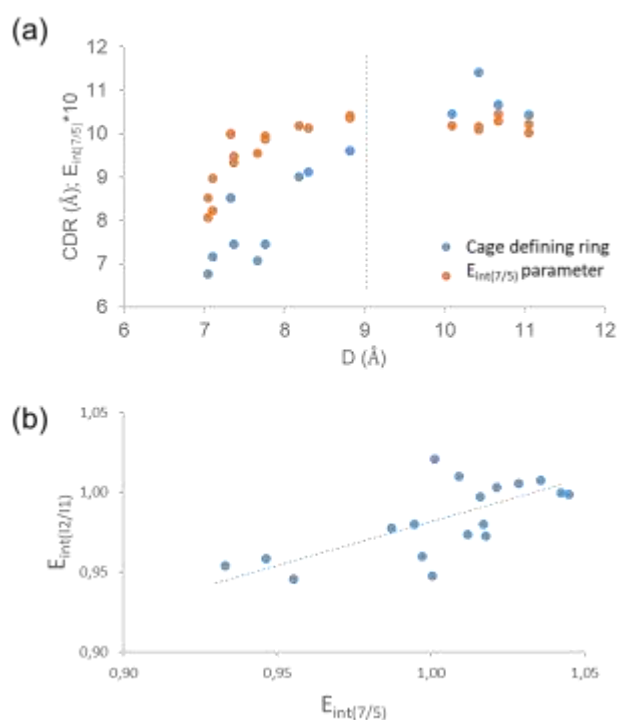

Figure 1. (a) Correlation between the diameter (D) of the largest sphere that can be included in small-pore cage-based zeolite structures and the cage-defining ring size (blue) or the $E_{int(7/5)}$ parameter (orange). (b) Correlation between the $E_{int(I2/I1)}$ and the $E_{int(7/5)}$ parameters.

Overall, these values suggest that the confinement effect associated to cage topology and its influence on the MTO product
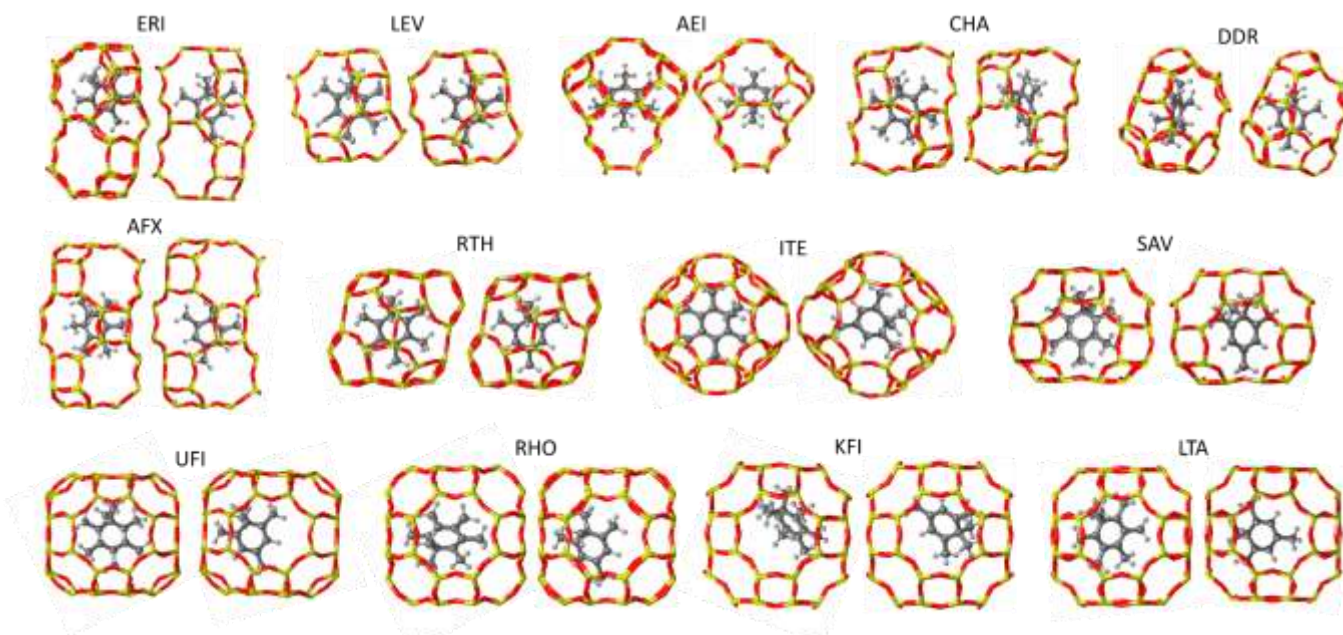
Figure 2. Optimized structures of 7MB$^+$ and 5MB$^+$ confined in pure silica periodic models of small-pore cage-based zeolites.

After the first ring-contraction step in the paring route, the bicycle-hexenyl I1 intermediate formed from I0 can directly decompose yielding propene or convert into a bulkier I2 intermediate precursor of iso-butene. In this case, and following the same approach used to quantify the relative contribution of the paring and side-chain routes, a $E_{int(I2/I1)}$ parameter calculated from the interaction energies of the I1 and I2 intermediates with different zeolite structures might provide an estimation of the relative amount of butene and propene that could be expected when using a particular microporous catalyst, assuming that the reaction follows the aromatic-based mechanism. The optimized geometries of the I1 and I2 intermediates allocated in the ERI, LEV, AEI, CHA, DDR, AFX, RTH, ITE, SAV, UFI, RHO, KFI, and LTA zeolite structures are depicted in Figure 3, and the calculated parameters are summarized in Table 1. Since the two intermediates contain a fully-methylated cyclopentenyl ring and the same number of atoms arranged in a different way, the influence of cavity topology on the $E_{int(I2/I1)}$ values in Table 1 is not so evident. Moreover, the values for ERI and LEV are not relevant because in these structures the 7MB$^+$ intermediate precursor of I1 and I2 is sterically destabilized and therefore the contribution of the paring route should be low. The plot in Figure 1b shows that there is a correlation between the $E_{int(I2/I1)}$ and the $E_{int(7/5)}$ parameters for all the structures in which the 7MB$^+$ intermediate can be stabilized, suggesting that as the $E_{int(7/5)}$ parameter increases and the paring route becomes predominant, the relative ratio of butene/propene formed should also increase.

Next, a systematic evaluation of the catalytic performance of zeolites with the LEV, CHA, AEI, RTH, ITE and LTA structures with different physicochemical properties, as well as samples of SAPO-34 and SAPO-18 with the CHA and AEI structures was performed to establish the trends in MTO product distribution. The as-synthesized small-pore zeolites and SAPOs show the characteristic powder X-ray diffraction (PXRD) patterns of LEV, CHA, AEI, RTH, ITE and LTA structures (Figure S2), and their crystal size (Figure S3) and chemical composition varies depending on the method of synthesis used, as indicated in Table S2.

Two samples of zeolite H-SSZ-13 with Si/Al molar ratios of ~15 and crystal sizes of ~1 µm (CHA_1) and ~70 nm (CHA_2), and a sample of isostructural H-SAPO-34 (CHA_3) consisting of crystals of ~1 µm with a (Al+P)/Si molar ratio of ~10 were prepared. For the AEI crystallographic structure, we synthesized two samples of zeolite H-SSZ-39 with Si/Al molar ratios of ~9 and crystal sizes of ~0.7 µm (AEI_1) and ~60 nm (AEI_2), and two samples of H-SAPO-18 with a (Al+P)/Si molar ratio of ~11-13 and crystals of ~150 nm (AEI_3) and ~0.8 µm (AEI_4). Zeolite H-RUB-13 was prepared either as nanocrystallites of ~80 nm with a Si/Al ratio of ~16 (RTH_1) or as micron-sized particles of 1-2 µm and a slightly lower Al content (RTH_2). Zeolite H-SSZ-17 with the LEV structure was synthesized in the form of small crystals of ~70 nm with a Si/Al molar ratio of 9, while ITE and LTA were obtained as intermediate (ITE, 0.5 × 0.2 µm) and large (LTA, 3-4 µm) crystals with Si/Al molar ratios of 13 and 20, respectively (Table S2). The textural properties of the calcined materials determined by N$_2$ adsorption experiments are analogous to those reported in the literature (Table S2), and the ^{29}Si and ^{27}Al MAS NMR spectra indicate that most of the Si and Al species remain in tetrahedral coordination within the respective zeotype and zeolite frameworks (Figure S4).

The catalytic performance of all these samples in the MTO reaction was tested at 623 K and 673 K with a WHSV of 0.8 h^{-1}, and the methanol conversion and product distribution results are summarized in Table 2 and plotted in Figures 4 and S5-S23 in the Supporting Information. In agreement with previous studies, when comparing catalyst with the same crystallographic structure and chemical composition but different physicochemical properties (CHA_1 with CHA_2, AEI_1 with AEI_2, AEI_3 with AEI_4, or RTH_1 with RTH_2), larger catalyst lifetimes are observed for the samples with smaller particle size. However, the light olefin product distribution remains mostly unaltered in these cases, and only varies when the microporous structure of the catalyst is different (Table 2 and S2).
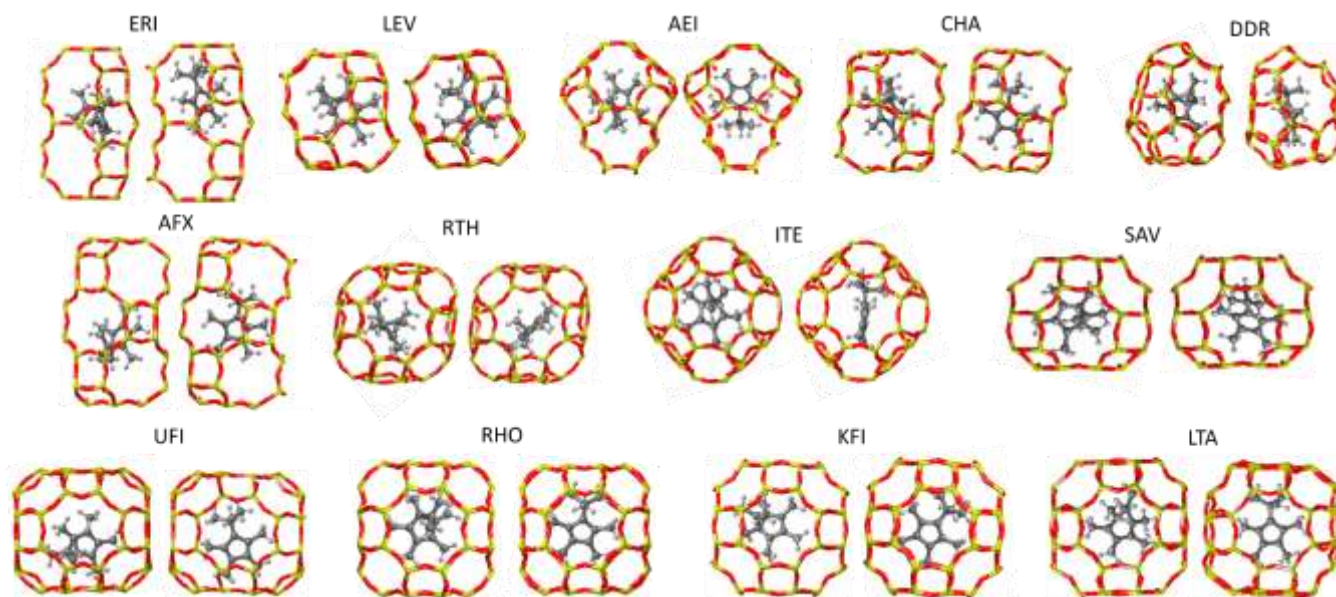
4

Figure 3. Optimized structures of I1 and I2 intermediates confined in pure silica periodic models of small-pore cage-based zeolites.
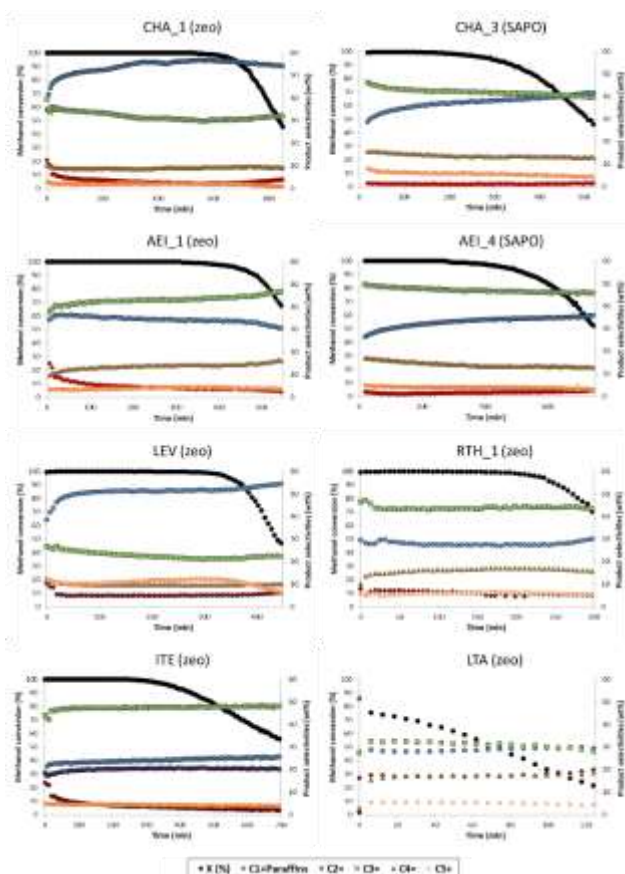

Figure 4. Methanol conversion and product selectivities (%wt) with time on stream (TOS) using small-pore cage-based zeolites and zeotypes. Reaction conditions: T=673 K, WHSV=0.8 h⁻¹, wcat=50 mg).

When comparing catalysts with the same structure but different framework composition, that is, isostructural zeolites and SAPOs, a relevant effect appears in the case of CHA, but not in the case of AEI. Thus, the $C_3^=/C_2^=$ and $(C_4^=+C_3^=)/C_2^=$ ratios obtained with H-SAPO-34 are twice as high as achieved with the isostructural zeolite H-SSZ-13, while all the values measured for either H-SSZ-39 or H-SAPO-18 are nearly equivalent (see Table 2). Finally, it should be noted that the selectivity values and the $C_3^=/C_2^=$ and $(C_4^=+C_3^=)/C_2^=$ ratios for any given catalyst are not the same at 623 and 673 K because the relative reaction rates change with temperature. However, the trends in selectivity are not modified, and the production of propene and butene via the paring route increases according to LEV < CHA (zeolite) < CHA (SAPO) < LTA ~ AEI (zeolite or SAPO) < RTH ~ ITE (see Table 2).

Following the hypothesis that the differences in selectivity arise from the preferential stabilization of 5MB⁺ or 7MB⁺ cations in the cavities and the associated enhancement of either the side-chain pathway leading to ethene or the paring route producing propene and butene, we searched for a correlation between the $C_3^=/C_2^=$ and $(C_4^=+C_3^=)/C_2^=$ ratios obtained for zeolites and zeotypes listed in Table 2 and the $E_{int(7/5)}$ parameters given in Table 1.

The plots in Figure 5 show that there is indeed a relationship, with the LEV structure with the smallest $E_{int(7/5)}$ value producing more ethene and with the largest $C_3^=/C_2^=$ and $(C_4^=+C_3^=)/C_2^=$ ratios found for the RTH and ITE structures, both of them with a $E_{int(7/5)}$ value larger than 1.01 (Table 1). Interestingly, the zeolite structure with the largest cavity, LTA, does not produce the maximum amount of propene and butene among the samples studied. Instead, its catalytic performance regarding olefin product distribution is quite similar to that of AEI, as could be expected from their corresponding $E_{int(7/5)}$ parameters, 1.00 in both cases. It is also important to remark that the different selectivity obtained with H-SSZ-13 zeolite and the isostructural H-SAPO-34, recently explained in terms of the larger flexibility of the AlPO framework that facilitates the accommodation of the bulkier 7MB⁺ intermediate,[17] is well represented by the correlations in Figure 5, as well as the equivalent performance of isostructural H-SSZ-39 and H-SAPO-18.
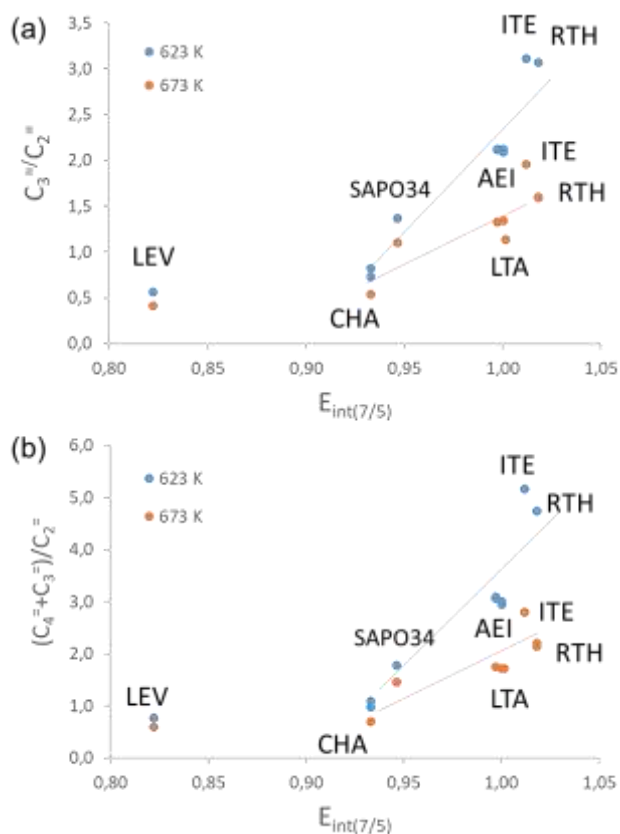
5

Figure 5. Relationships between the measured (a) $C_3^=/C_2^=$ and (b) $(C_4^=+C_3^=)/C_2^=$ ratios and the $E_{int(7/5)}$ parameter in different small-pore cage-based zeolites and zeotypes. Reaction conditions: T=623 or 673 K, WHSV=0.8 h^{-1}.

However, the relative amount of propene and butene detected in the LEV sample, with the smallest cavity and the smallest $E_{int(7/5)}$ value, is clearly larger than expected according to these relationships. As mentioned before, the cavity in LEV is too small to host the fully-methylated 7MB$^+$ intermediate involved in the paring route (see interaction energies in Table S1) and the value of the $E_{int(7/5)}$ parameter, 0.822, indicates that 5MB$^+$ will be the most abundant aromatic hydrocarbon pool species in LEV, in agreement with previous ^{13}C NMR and GC-MS studies.[8] Therefore, in the absence of 7MB$^+$ due to steric constraints, propene and butene in LEV must be formed through the alkene-based cycle of the MTO mechanism (see Scheme 1) while ethene is obtained via the side-chain pathway of the aromatics-based cycle. A deeper inspection of the product distribution in Figure 4 shows a larger contribution of pentenes and higher olefins in LEV (~12%) than in any other catalyst (< 6%), further supporting the alkene-based cycle as the main mechanism operating in the smallest cages. On the other hand, the formation of C1 and alkanes (red rhombus in Figure 4) is below 5% in all catalysts tested except LTA, where the amount of paraffins is comparable to that of butenes, both of them over 16%. The higher production of alkanes in LTA might be related to the size of the cavity, large enough to accommodate bulky intermediates or transition states participating in hydrogen transfer processes.[33]

Finally, a linear trend was also observed between the measured $C_4^=/C_3^=$ ratios and the calculated $E_{int(l2/l1)}$ parameter for all structures in which propene and butene are mostly formed through the paring route of the aromatic-based cycle (see Figure S24 in the Supporting Information).

In a last step, and to further check the validity of the hypothesis behind the $E_{int(7/5)}$ parameter to rationalize the MTO selectivity and to set the limits of its applicability, the larger set of experimental data from ref. [14] were represented in Figure 6 against the $E_{int(7/5)}$ parameter. Both the $C_3^=/C_2^=$ (in blue) and the $(C_4^=+C_3^=)/C_2^=$ ratios (in orange) follow the trends described for the experimental data presented in this work, and the existence of two types of materials is clearly observed. On one hand, the group of zeolite structures with diameter of cavity smaller than ~9 Å and with a tight fitting between the cage topology and the entrapped methylbenzenium cations, plotted as squares in Figure 6. This group includes AEI, CHA, DDR, AFX, RTH and ITE, with $E_{int(7/5)}$ values between 0.9 and 1.01, and in them the confinement effect determines the relative stability of 7MB$^+$ and 5MB$^+$ cations and the olefin product distribution. On the other hand, there is a group of cage-based zeolites with larger cavities in their structure (SAV, UFI, RHO, KFI or LTA, depicted as circles in Figure 6) in where the confinement effect is partly lost and other competitive processes start to take place. In this last case, linear correlations with the $E_{int(7/5)}$ parameter are still observed, but the amount of propene and butene detected is lower because of the competing processes leading to alkanes.
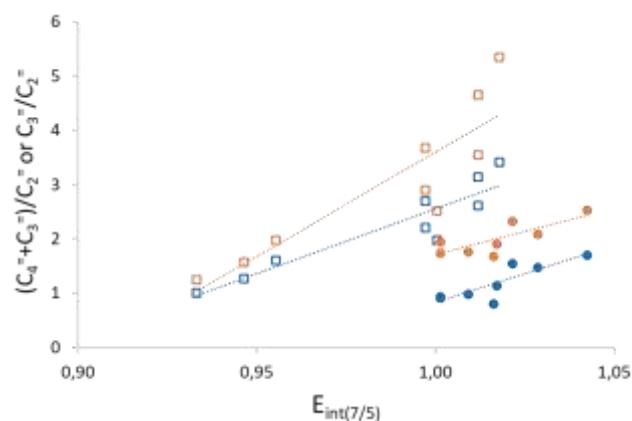

Figure 6. Relationships between experimental $C_3^=/C_2^=$ (blue) and $(C_4^=+C_3^=)/C_2^=$ (orange) ratios from ref. [14] and the $E_{int(7/5)}$ parameter. Squares and circles correspond to structures with cavity diameter smaller and larger than ~9 Å, respectively. Reaction conditions: T= 673 K, WHSV=1.3 h^{-1}.

Conclusion

The product distribution of the MTO reaction catalyzed by small-pore cage-based zeolites depends on the ability of the catalyst cages to preferentially stabilize the 5MB$^+$ cations involved in the side-chain pathway producing ethene or the fully methylated 7MB$^+$ cation leading to propene and butene via the paring route. The relative stabilization by confinement of these two intermediates in a series of zeolite structures containing cavities of different dimensions and topology has been evaluated by means of periodic DFT calculations, and the quantitative $E_{int(7/5)}$ parameter has been obtained for ERI, LEV, AEI, CHA, DDR, AFX, RTH, ITE, SAV, UFI, RHO, KFI, and LTA zeolite structures. Some of these catalysts have been synthesized with different physicochemical properties and composition, and their catalytic performance in the MTO reaction has been tested. By combining

the theoretical data and the results from the catalytic experiments, the limits of the $E_{int(7/5)}$ parameter as predictor of product distribution in the MTO reaction have been established. Thus, in the small cages of ERI and LEV structures, with $E_{int(7/5)}$ values below 0.9, the bulky 7MB+ is sterically forbidden and propene and higher alkenes are formed through the alkene-based catalytic cycle. In contrast, in the zeolite structures with $E_{int(7/5)}$ values larger than 0.9, propene and butene are formed through the paring mechanism, and the relative contribution of the paring and side-chain pathways directly correlates with the $E_{int(7/5)}$ parameter. However, there are clear differences between the structures with a tight fitting between the entrapped methylbenzenium cations and the hosting cavity (CHA, AEI, DDR, RTH and ITE, with $E_{int(7/5)}$ values between 0.9 and 1.01) and those with larger cages in where the confinement effect is lost in part and other competitive processes such as hydrogen transfer start to take place (SAV, UFI, RHO, KFI or LTA, with $E_{int(7/5)}$ values > 1). In this last case, the distribution of the light olefins still correlates with the $E_{int(7/5)}$ parameter, but the formation of alkanes and other products is significant.

Experimental Section

Computational Details. All calculations are based on periodic density functional theory (DFT) and were performed using the Perdew−Burke−Ernzerhof (PBE) exchange-correlation functional within the generalized gradient approach (GGA),[34,35] as implemented in the Vienna Ab-initio Simulation Package (VASP) code.[36] The valence density was expanded in a plane wave basis set with a kinetic energy cutoff of 600 eV, and the effect of the core electrons in the valence density was taken into account by means of the projected augmented wave (PAW) formalism.[37] Integration in the reciprocal space was carried out at the Γ k-point of the Brillouin zone. Dispersion corrections to the energies were evaluated using the DFT-D Grimme's method.[38,39]

The pure silica and pure aluminophosphate (AlPO) models of ERI, LEV, AEI, CHA, DDR, AFX, RTH, ITE, SAV, UFI, RHO, KFI, and LTA structures were generated by optimizing the unit cell parameters and atomic positions of the experimental structures reported in the IZA database[32] with the computational setup described above. Then, keeping the unit cell parameters fixed, one cationic intermediate was placed in each unit cell and the positions of all atoms in the system were fully optimized without restrictions. The interaction energies E_{int} were calculated as the difference in energy between the global system composed by the cationic intermediate inside the zeolite or zeotype model and the sum of the energies of the empty catalyst and the isolated cation. The interaction energy ratio parameters $E_{int(7/5)}$ and $E_{int(I2/I1)}$ were calculated as:

$$E_{int(7/5)} = E_{int}(7MB·)/E_{int}(5MB·)$$
$$E_{int(I2/I1)} = E_{int}(I2·)/E_{int}(I1·)$$

Synthesis of the organic structure-directing agents (OSDAs). The synthesis of N-methyl quinuclidinium (MeQUIN), N,N-dimethyl-3,5-dimethylpiperidinium (DMDP), 1,2,3,4,5-pentamethyl-1H-imidazol-3-ium (PMI), methyltert-butylphosphonium (MTBP) and 1,2-dimethyl-3-(4-methylbenzyl)-1H-imidazol-3-ium (DMMBI) organic structure-directing agents is described in detail in the Supporting Information.

Synthesis of Zeolites and zeotypes. Different cage-based small pore zeolites and SAPOs with the LEV, CHA, AEI, RTH, ITE and LTA frameworks with different physicochemical properties were synthesized following procedures from the literature.[15,40-44] Experimental details for each synthesis can be found in the Supporting Information.

Characterization. Powder X-ray diffraction (PXRD) measurements were performed with a multisample Philips X'Pert diffractometer equipped with a graphite monochromator, operating at 40 kV and 35 mA, and using Cu Kα radiation (λ = 0.1542 nm). The morphology and particle size of the zeolites were characterized by Scanning Electron Microscope (SEM, JEOL JSM-6300). The chemical composition of the solid samples was determined by inductively coupled plasma atomic absorption spectroscopy (ICP-OES) using a Varian 715-ES. Textural properties were determined by N_2 adsorption isotherms measured at 77 K with a Micromeritics ASAP 2020. Solid state MAS NMR spectra were recorded with a Bruker AV400 III HD spectrometer. ^{27}Al MAS NMR spectra were recorded at spinning rate of 20 kHz with a 90° pulse length of 0.5 μs with 1 s repetition time. The ^{27}Al chemical shift was referred to $Al^{3+}(H_2O)_6$. ^{29}Si MAS NMR spectra were recorded at spinning rate of 5 kHz at 79.459 MHz with a 55° pulse length of 3.5 μs and a repetition time of 180 s. ^{29}Si chemical shift was referenced to tetramethylsilane.

Catalytic tests. The catalyst was pelletized, crushed and sieved into 0.2-0.4 mm particle size. 50 mg of sample was mixed with 2 g quartz (Fluka) before being introduced into the fixed-bed reactor (7 mm diameter). N_2 (30 mL/min) was bubbled in methanol held at 256 K, giving a WHSV = 0.8 h^{-1}. The catalyst was first activated with a nitrogen flow of 80 mL/min for 1 h at 813 K, and then the temperature was decreased to reaction conditions (623 or 673 K). Each experiment was analyzed every 5 min with an online gas chromatograph (Bruker 450GC, with PONA and Al_2O_3-Plot capillary columns, and two FID detectors). Conversion and selectivity were considered in carbon basis.
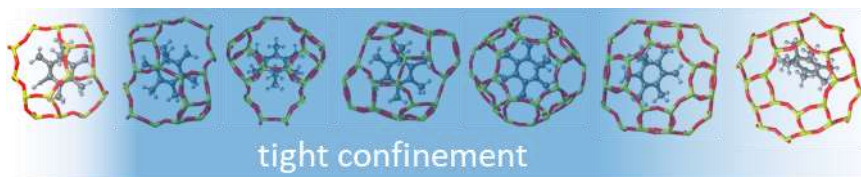
[1]   G. A. Olah, *Angew. Chemie Int. Ed.* **2005**, *44*, 2636–2639.
[2]   P. Tian, Y. Wei, M. Ye, Z. Liu, *ACS Catal.* **2015**, *5*, 1922–1938.

[3]   M. Moliner, C. Martínez, A. Corma, *Chem. Mater.* **2014**, *26*, 246–258.

[4]   J. F. Haw, W. Song, D. M. Marcus, J. B. Nicholas, *Acc. Chem. Res.* **2003**, *36*, 317–326.

[5]   U. Olsbye, S. Svelle, M. Bjørgen, P. Beato, T. V. W. Janssens, F. Joensen, S. Bordiga, K. P. Lillerud, *Angew. Chemie Int. Ed.* **2012**, *51*, 5810–5831.

[6]   V. Van Speybroeck, K. De Wispelaere, J. Van der Mynsbrugge, M. Vandichel, K. Hemelsoet, M. Waroquier, *Chem. Soc. Rev.* **2014**, *43*, 7326–7357.

[7]   I. Yarulina, A. D. Chowdhury, F. Meirer, B. M. Weckhuysen, J. Gascon, *Nat. Catal.* **2018**, *1*, 398–411.

[8]   J. Li, Y. Wei, J. Chen, S. Xu, P. Tian, X. Yang, B. Li, J. Wang, Z. Liu, *ACS Catal.* **2015**, *5*, 661–665.

[9]   W. Zhang, J. Chen, S. Xu, Y. Chu, Y. Wei, Y. Zhi, J. Huang, A. Zheng, X. Wu, X. Meng, F. Xiao, F. Deng, Z. Liu, *ACS Catal.* **2018**, *8*, 10950–10963.

[10]   I. Pinilla-Herrero, U. Olsbye, C. Márquez-Álvarez, E. Sastre, *J. Catal.* **2017**, *352*, 191–207.

[11]   I. Pinilla-Herrero, C. Márquez-Álvarez, E. Sastre, *Catal. Sci. Technol.* **2017**, *7*, 3892–3901.

[12]   Y. Bhawe, M. Moliner-Marin, J. D. Lunn, Y. Liu, A. Malek, M. Davis, *ACS Catal.* **2012**, *2*, 2490–2495.

[13]   J. H. Kang, R. Walter, D. Xie, T. Davis, C.-Y. Chen, M. E. Davis, S. I. Zones, *ChemPhysChem* **2018**, *19*, 412–419.

[14]   J. H. Kang, F. H. Alshafei, S. I. Zones, M. E. Davis, *ACS Catal.* **2019**, *9*, 6012–6019.

[15]   C. Li, C. Paris, J. Martínez-Triguero, M. Boronat, M. Moliner, A. Corma, *Nat. Catal.* **2018**, *1*, 547–554.

[16]   P. Ferri, C. Li, C. Paris, A. Vidal-Moya, M. Moliner, M. Boronat, A. Corma, *ACS Catal.* **2019**, *9*, 11542–11551.

[17]   P. Ferri, C. Li, R. Millán, J. Martínez- Triguero, M. Moliner, M. Boronat, A. Corma, *Angew. Chemie Int. Ed.* **2020**, anie.202007609.

[18]   S. Teketel, U. Olsbye, K.-P. Lillerud, P. Beato, S. Svelle, *Microporous Mesoporous Mater.* **2010**, *136*, 33–41.

[19]   I. Lezcano-Gonzalez, E. Campbell, A. E. J. Hoffman, M. Bocus, I. V. Sazanovich, M. Towrie, M. Agote-Aran, E. K. Gibson, A. Greenaway, K. De Wispelaere, V. Van Speybroeck, A. M. Beale, *Nature Materials* **2020**, *19*, 1081–1087.

[20]   N. Wang, Y. Zhi, Y. Wei, W. Zhang, Z. Liu, J. Huang, T. Sun, S. Xu, S. Lin, Y. He, A. Zheng, Z. Liu, *Nature Commun.* **2020**, *11*, 1079-1090. 11564–11568.

[21]   J. Li, Y. Wei, J. Chen, P. Tian, X. Su, S. Xu, Y. Qi, Q. Wang, Y. Zhou, Y. He, Z. Liu, *J. Am. Chem. Soc.* **2012**, *134*, 836–839.

[22]   S. Xu, A. Zheng, Y. Wei, J. Chen, J. Li, Y. Chu, M. Zhang, Q. Wang, Y. Zhou, J. Wang, F. Deng, Z. Liu, *Angew. Chemie Int. Ed.* **2013**, *52*, 11564–11568.

[23]   C. M. Wang, Y. D. Wang, Z. K. Xie, *Catal. Sci. Technol.* **2014**, *4*, 2631-2638.

[24]   C. M. Wang, Y. D. Wang, Y. J. Du, G. Yang, Z. K. Xie, *Catal. Sci. Technol.* **2015**, *5*, 4354-4364.

[25]   D. M. McCann, D. Lesthaeghe, P. W. Kletnieks, D. R. Guenther, M. J. Hayman, V. Van Speybroeck, M. Waroquier, J. F. Haw, *Angew. Chemie Int. Ed.* **2008**, *47*,

5179–5182.

[26]   K. De Wispelaere, K. Hemelsoet, M. Waroquier, V. Van Speybroeck, *J. Catal.* **2013**, *305*, 76–80.

[27]   K. Hemelsoet, J. Van der Mynsbrugge, K. De Wispelaere, M. Waroquier, V. Van Speybroeck, *ChemPhysChem* **2013**, *14*, 1526–1545.

[28]   S. Ilias, A. Bhan, *ACS Catal.* **2013**, *3*, 18–31.

[29]   W. Song, H. Fu, J. F. Haw, *J. Am. Chem. Soc.* **2001**, *123*, 4749–4754.

[30]   S. Svelle, U. Olsbye, F. Joensen, M. Bjørgen, *J. Phys. Chem. C* **2007**, *111*, 17981–17984.

[31]   A. Hwang, B. A. Johnson, A. Bhan, *J. Catal.* **2019**, *369*, 86–94.

[32]   IZA Database of Zeolite Structures. http://www.iza-structure.org/

[33]   S. Müller, Y. Liu, F. M. Kirchberger, M. Tonigold, M. Sanchez-Sanchez, J. A. Lercher, *J. Am. Chem. Soc.* **2016**, *138*, 15994-16003.

[34]   J. P. Perdew, K. Burke, M. Ernzerhof, *Phys. Rev. Lett.* **1996**, *77*, 3865–3868.

[35]   J. P. Perdew, K. Burke, M. Ernzerhof, *Phys. Rev. Lett.* **1997**, *78*, 1396–1396.

[36]   G. Kresse, J. Furthmüller, *Phys. Rev. B* **1996**, *54*, 11169–11186.

[37]   P. E. Blöchl, *Phys. Rev. B* **1994**, *50*, 17953–17979.

[38]   S. Grimme, *J. Comput. Chem.* **2004**, *25*, 1463–1473.

[39]   S. Grimme, *J. Comput. Chem.* **2006**, *27*, 1787–1799.

[40]   N. Martín, Z. Li, J. Martinez-Triguero, J. Yu, M. Moliner, A. Corma, *Chem. Commun.* **2016**, *52*, 6072−6075.

[41]   E. M. Gallego, C. Li, C. Paris, N. Martin, J. Martinez-Triguero, M. Boronat, M. Moliner, A. Corma, *Chem. − Eur. J.* **2018**, *24*, 14631−14635.

[42]   R. Martínez-Franco, Z. Li, J. Martínez-Triguero, M. Moliner, A. Corma. *Catal. Sci. Tecnol.* **2016**, *6*, 2796-2806.

[43]   C. V. Tuoto, J. B. Nagy A. Nastro, *Stud. Surf. Sci. Catal.* **1997**, *105*, 213-220.

[44]   B. W. Boal, J. E: Schmidt, M. A. Deimund, M. W. Deem, L. M. Henling, S. K. Brand, S. I. Zones, M. E. Davis, *Chem. Mater.* **2015**, *27*, 7774-7779.

.

Entry for the Table of Contents

tight confinement

The limits of the confinement effect associated to cage topology to control de MTO product distribution in small-pore cage-based zeolites is explored for a series of zeolite and zeotype structures containing small cages where steric constraints might change the mechanism, and large cavities where confinement effects are partly lost.